

Two Dimensional Electromagnetic Scattering from Dielectric Objects using Quantum Lattice Algorithm

George Vahala¹, Min Soe², Linda Vahala³, and Abhay K. Ram⁴

¹Department of Physics, William & Mary, Williamsburg, VA23185

²Department of Mathematics and Physical Sciences, Rogers State University, Claremore, OK 74017

³Department of Electrical & Computer Engineering, Old Dominion University, Norfolk, VA 12319

⁴Plasma Science and Fusion Center, MIT, Cambridge, MA 02139

October 13, 2021

Abstract: Detailed simulations are presented on a quantum lattice algorithm (*QLA*) for the solution of pulse propagation in a two dimensional (2D) refractive index medium. In particular, the initial value problem of an electromagnetic pulse scattering from a localized dielectric object is considered. The properties of the scattered waves depend on the scale length of the transition layer separating the vacuum from the core of the dielectric. The *QLA* perturbatively recovers the Maxwell equations to second order in a perturbation parameter ε that is just the normalized initial speed of light. *QLA* simulations show that the Maxwell equations are still recovered when $\varepsilon = 1$.

1 Introduction

It is important to develop algorithms that are not only ideally parallelized on classical supercomputers but which, with a little tweaking, can also be run on error-correcting quantum computers. One class of such mesoscopic algorithms is the quantum lattice algorithm (*QLA*) [1-20]. *QLA* typically consists of an interleaved sequence of unitary collision and streaming operators acting on some appropriate basis set (like a set of qubits). Under appropriate moments and in the continuum limit the *QLA* can be so chosen that it will recover the desired continuum equations to be studied. In particular, *QLA* were developed for the solution of one-dimensional (1D) soliton dynamics for the nonlinear Schrodinger equation (*NLS*) and the Korteweg-De Vries (*KdV*) equations [6, 9-11]. Different choice of unitary collision operators are needed to, for example, recover the $\partial^2/\partial x^2$ for *NLS* or remove this second derivative but have instead the $\partial^3/\partial x^3$ for *KdV*.

The application of quantum information science to plasma physics has drawn interest in recent years [21-24]. Electromagnetic waves are ubiquitous in laboratory, space, and astrophysical plasmas. The waves can be externally generated by an antenna and coupled to a plasma, or internally generated by a plasma instability. In either case, an analysis of the propagation and damping of waves is essential – whether for determining the spatial profile of power deposition or for diagnosing the interior of a hot plasma. The allure for developing a *QLA* for electromagnetic wave propagation is the connection between the relativistically invariant Maxwell equations and the Dirac equation

for a relativistic particle [25-27]. Following this connection, Khan [28] has used the Riemann-Silberstein-Weber vectors to express Maxwell equations, for an inhomogeneous scalar dielectric medium, as a matrix evolution equation of an 8-spinor. However, this 8-spinor evolution equation is not fully unitary; the operators which include the derivative of the refractive index are Hermitian. For a homogeneous dielectric medium, the 8-spinor representation decouples into two independent 4-spinor equations which are fully unitary. The backbone of the QLA for Maxwell equations is the realization that, for a homogeneous medium, the 4-spinor representation has the same structure as the Dirac equation for a massless free particle[1, 17]. The only difference being in the linear couplings of the spinor components. Thus, we are able to generalize Yezep's [1] QLA construction for the Dirac equation to construct the required unitary collision operator which recovers Maxwell equations to second order accuracy in terms of a small parameter introduced in the collision angle.

For wave propagation in one spatial dimension in a medium with spatially varying index of refraction along the same direction, we have recently developed a QLA for Maxwell equations [17, 29]. This QLA was used to study the propagation of an electromagnetic pulse from vacuum through a dielectric slab. The classic textbook version of this problem is the incidence of a plane wave onto an interface separating two different dielectric media. The reflection and transmission of the incident plane wave at the interface is obtained by applying the boundary conditions that follow from Maxwell equations [31]. For a plane wave propagating from medium with refractive index n_1 through the interface to a medium with refractive index n_2 , we find that,

$$\frac{E_{refl}}{E_{inc}} = \frac{n_1 - n_2}{n_1 + n_2} \quad , \quad \frac{E_{trans}}{E_{inc}} = \frac{2n_1}{n_1 + n_2}$$

where E_{inc} , E_{refl} , and E_{trans} are the electric field amplitudes of the incident, reflected, and transmitted plane waves, respectively. Our 1D QLA simulation differs from this classic example in two ways. First, the QLA simulation is for a spatially localized pulse instead of a plane wave. Second, we do not impose any boundary conditions – the QLA simulation is the space-time evolution of an initial pulse that is launched in medium n_1 and propagates towards medium n_2 . From the QLA simulations, we realized there are significant differences from the boundary value plane wave problem: the pulse has finite width and at a particular time it will straddle the boundary layer region and have a part of the pulse in medium n_1 and part of it in medium n_2 . Interestingly, while the ratio of the reflected to the incident electric field amplitudes was the same as for the plane waves, the QLA simulations showed that the ratio of the transmitted to incident electric field amplitudes was different. From the QLA simulations,

$$\frac{E_{refl}}{E_{inc}} = \frac{n_1 - n_2}{n_1 + n_2} \quad , \quad \frac{E_{trans}}{E_{inc}} = \frac{2n_1}{n_1 + n_2} \sqrt{\frac{n_2}{n_1}}$$

The QLA simulations gave this extra factor of $\sqrt{n_2/n_1}$ for different choices of n_1 and n_2 as well as for different pulse geometry. We then developed a theory for Gaussian pulses to show that this extra factor of $\sqrt{n_2/n_1}$ is present in the ratio of the transmitted to incident pulse amplitudes [29].

Here we are concerned with developing a 2D QLA and performing QLA simulations for the propagation of a 1D electromagnetic pulse in the x -direction and incident onto a 2D localized dielectric medium of refractive index $n(x, z)$. In Sec. 2 we summarize the Khan 8-spinor representation of the inhomogeneous 2D Maxwell equations, while in Sec. 3 we discuss the details of the 2D QLA for $x - z$ dependent fields. In Sec. 4 we present details of the 2D QLA simulations off various dielectric geometries, showing cases where there is multiple internal reflections within the dielectric medium and conditions under which there are no significant internal reflections. We discuss the $\nabla \cdot \mathbf{B}$ condition (\mathbf{B} is the magnetic field) and the role of the collision angle perturbation

parameter ϵ and its interpretation as a normalized speed of light in the initial medium. In Sec. 5 we summarize the conclusions from our simulations.

2 Khan [28] representation of Maxwell Equations in a Scalar Dielectric Medium

First one rewrites the Maxwell equations utilizing the Riemann-Silberstein-Weber vectors

$$\mathbf{F}^\pm = \sqrt{\epsilon}\mathbf{E} \pm i\frac{\mathbf{B}}{\sqrt{\mu_0}}. \quad (1)$$

where ϵ is the dielectric constant and μ_0 the magnetic permeability. Here we will consider a scalar dielectric medium $\epsilon = \epsilon(\mathbf{x})$, and with $\mu_0 = \text{const}$. \mathbf{E} is the (real) electric field, and \mathbf{B} the magnetic flux density, with the electric displacement $\mathbf{D} = \epsilon\mathbf{E}$, and the magnetic field $\mathbf{H} = \mathbf{B}/\mu_0$. The Maxwell equations (with free charge density ρ_f and free current density \mathbf{J}_f)

$$\nabla \cdot \mathbf{D} = \rho_f \quad \nabla \cdot \mathbf{B} = 0 \quad (2)$$

$$\nabla \times \mathbf{E} = -\frac{\partial \mathbf{B}}{\partial t} \quad \nabla \times \mathbf{H} = \mathbf{J}_f + \frac{\partial \mathbf{D}}{\partial t} \quad (3)$$

can be written in the Riemann-Silberstein-Weber form [28],

$$i\frac{\partial \mathbf{F}^\pm}{\partial t} = \pm v_{ph} \nabla \times \mathbf{F}^\pm \pm \frac{1}{2} \nabla v_{ph} \times (\mathbf{F}^\pm + \mathbf{F}^\mp) - iv_{ph} \sqrt{\frac{\mu_0}{2}} \mathbf{J}_f, \quad (4)$$

$$\nabla \cdot \mathbf{F}^\pm = \frac{1}{2v_{ph}} \nabla v_{ph} \cdot (\mathbf{F}^\pm + \mathbf{F}^\mp) + v_{ph} \sqrt{\frac{\mu_0}{2}} \rho_f. \quad (5)$$

where v_{ph} is the normalized electromagnetic phase velocity of the wave in the medium

$$v_{ph} = \frac{1}{\sqrt{\epsilon\mu_0}} \quad (6)$$

Note that the coupling between the two field polarizations \mathbf{F}^\pm occurs through the inhomogeneity in the refractive index $n(\mathbf{x}) = \sqrt{\epsilon(\mathbf{x})}$.

These equations can be written in terms of the time evolution of the 8-spinor

$$\Psi^\pm = \begin{pmatrix} -F_x^\pm \pm iF_y^\pm \\ F_z^\pm \\ F_z^\pm \\ F_x^\pm \pm iF_y^\pm \end{pmatrix}, \quad (7)$$

which, on assuming there are no free charges or currents ($\rho_f = 0$, $\mathbf{J}_f = 0$), reduces to

$$\frac{\partial}{\partial t} \begin{pmatrix} \Psi^+ \\ \Psi^- \end{pmatrix} = -v_{ph} \begin{pmatrix} \mathbf{M} \cdot \nabla - \Sigma \cdot \frac{\nabla \epsilon}{4\epsilon} & +iM_z \Sigma \cdot \frac{\nabla \epsilon}{2\epsilon} \alpha_y \\ +iM_z \Sigma^* \cdot \frac{\nabla \epsilon}{2\epsilon} \alpha_y & \mathbf{M}^* \cdot \nabla - \Sigma^* \cdot \frac{\nabla \epsilon}{4\epsilon} \end{pmatrix} \begin{pmatrix} \Psi^+ \\ \Psi^- \end{pmatrix}. \quad (8)$$

The \mathbf{M} matrices are the tensor products of the Pauli spin matrices, $\boldsymbol{\sigma} = (\sigma_x, \sigma_y, \sigma_z)$. with the 2×2 identity matrix \mathbf{I}_2 :

$$\mathbf{M} = \boldsymbol{\sigma} \otimes \mathbf{I}_2, \quad \text{so that} \quad M_z = \sigma_z \otimes \mathbf{I}_2. \quad (9)$$

where

$$\sigma_x = \begin{pmatrix} 0 & 1 \\ 1 & 0 \end{pmatrix}, \quad \sigma_y = \begin{pmatrix} 0 & -i \\ i & 0 \end{pmatrix}, \quad \sigma_z = \begin{pmatrix} 1 & 0 \\ 0 & -1 \end{pmatrix}. \quad (10)$$

The 4×4 matrices $\boldsymbol{\alpha}$ and $\boldsymbol{\Sigma}$ are defined by,

$$\boldsymbol{\alpha} = \begin{pmatrix} 0 & \boldsymbol{\sigma} \\ \boldsymbol{\sigma} & 0 \end{pmatrix}, \quad \boldsymbol{\Sigma} = \begin{pmatrix} \boldsymbol{\sigma} & 0 \\ 0 & \boldsymbol{\sigma} \end{pmatrix}. \quad (11)$$

We shall perform two-dimensional (2D) simulations of a Gaussian electromagnetic pulse propagating from a vacuum and interacting with a localized 2D refractive index. We shall take the refractive index $n = n(x, z)$, so that the 8-spinor evolution equations reduce nicely to

$$\frac{\partial}{\partial t} \begin{bmatrix} q_0 \\ q_1 \\ q_2 \\ q_3 \end{bmatrix} = -\frac{1}{n(x, z)} \left(\frac{\partial}{\partial x} \begin{bmatrix} q_2 \\ q_3 \\ q_0 \\ q_1 \end{bmatrix} + \frac{\partial}{\partial z} \begin{bmatrix} q_0 \\ q_1 \\ -q_2 \\ -q_3 \end{bmatrix} \right) + \frac{\partial n / \partial x}{2n^2(x, z)} \begin{bmatrix} q_1 + q_6 \\ q_0 - q_7 \\ q_3 - q_4 \\ q_2 + q_5 \end{bmatrix} + \frac{\partial n / \partial z}{2n^2(x, z)} \begin{bmatrix} q_0 - q_7 \\ -q_1 - q_6 \\ q_2 + q_5 \\ -q_3 + q_4 \end{bmatrix} \quad (12)$$

$$\frac{\partial}{\partial t} \begin{bmatrix} q_4 \\ q_5 \\ q_6 \\ q_7 \end{bmatrix} = -\frac{1}{n(x, z)} \left(\frac{\partial}{\partial x} \begin{bmatrix} q_6 \\ q_7 \\ q_4 \\ q_5 \end{bmatrix} + \frac{\partial}{\partial z} \begin{bmatrix} q_4 \\ q_5 \\ -q_6 \\ -q_7 \end{bmatrix} \right) + \frac{\partial n / \partial x}{2n^2(x, z)} \begin{bmatrix} q_5 + q_2 \\ q_4 - q_3 \\ q_7 - q_0 \\ q_6 + q_1 \end{bmatrix} + \frac{\partial n / \partial z}{2n^2(x, z)} \begin{bmatrix} q_4 - q_3 \\ -q_5 - q_2 \\ q_6 + q_1 \\ -q_7 + q_0 \end{bmatrix}. \quad (13)$$

3 Quantum Lattice Algorithm (QLA) for 2D Maxwell Equations

3.1 Overview of QLA

It is convenient to use a Cartesian structure for QLA. Thus a 2D QLA reduces to the tensor product of two orthogonal 1D QLAs. Here, we will assume the electromagnetic fields are functions of (x, z, t) . The 1D QLA is an interleaved sequence of non-commuting collision-stream operators. The collision operator C entangles the qubits at each lattice site, while the streaming operator S spreads this entanglement throughout the lattice. The basic structure of the evolution operator consists of this interleaved sequence

$$\begin{aligned} U &= \bar{S}_- C \bar{S}_+ C^\dagger \cdot S_+ C S_- C^\dagger, \\ \bar{U} &= S_+ C^\dagger S_- C \cdot \bar{S}_- C^\dagger \bar{S}_+ C \end{aligned} \quad (14)$$

acting on a qubit vector Q . C^\dagger is the adjoint of C . The streaming operator S_+ streams half of the qubits of Q in the positive Cartesian direction, while leaving the other half of the qubits untouched. \bar{S}_+ now streams those qubits that S had left untouched. A small parameter ε is introduced into the unitary collision angle matrix - and we will discuss the significance of ε in a later section following the simulation results. The collision and streaming operators are so chosen that when

$$Q(t + \delta t) = \bar{U} U Q(t) \quad (15)$$

is expanded to second order in ε one will recover the required (1D) part of Eqs. (12) and (13) that involves the time and spatial derivative on Q . The remaining terms in Eqs. (12) and (13), those

involving the derivative on the refractive index, will be recovered by appropriate potential operator whose collision angle will also be dependent on ε .

Interestingly, the 2D QLA can use the same dimensionality of the qubit vector Q as in 1D - but, of course, now $Q = Q(x, z, t)$. With obvious notational generalization of Eq. (15), we have

$$Q(t + \delta t) = \bar{U}_Z U_Z \bar{U}_X U_X Q(t) \quad (16)$$

For appropriately chosen collision-stream operators one will recover the required $\partial/\partial t$, and the spatial derivative terms $\partial/\partial x$ and $\partial/\partial z$ in the long time - long spatial scale limit $\varepsilon \ll 1$.

To determine the collision operator for x-dependence, we note in Eqs. (12)-(13) that the qubit couplings of $\partial/\partial t$ with $\partial/\partial x$ requires the coupling of $q_0 - q_2, q_1 - q_3, q_4 - q_6, q_5 - q_7$. This can readily be achieved by an 8×8 collision matrix.

However to recover the coupling of $\partial/\partial t - \partial/\partial z$ in Eqs. (12)-(13) one sees that in the 8-qubit representation one has diagonal coupling $q_0 - q_0, q_1 - q_1, q_2 - q_2, \dots$. Since entanglement requires a collision operator to act on at least 2 qubits then we must move to a 16-qubit representation to recover z-dependence. This problem of diagonal coupling of an 8-qubit system can be traced back to the diagonal structure of the Pauli spin matrix σ_z . Since both U_X and U_Z act on the same qubit vector $Q(t)$, it is simplest for 2D QLA to work with a 16-component qubit vector.

3.2 16-qubit QLA for 1D x-propagation

A 16-qubit formulation for 1D QLA propagation in the x-direction can be determined from the unitary 16×16 collision matrix \bar{C}_X and the 8×8 submatrices C_{8X}

$$\bar{C}_X = \begin{bmatrix} C_{8X}(\theta) & 0 \\ 0 & C_{8X}(\theta) \end{bmatrix} \quad (17)$$

where

$$C_{8X}(\theta) = \begin{bmatrix} \cos \theta & 0 & 0 & 0 & \sin \theta & 0 & 0 & 0 \\ 0 & \cos \theta & 0 & 0 & 0 & \sin \theta & 0 & 0 \\ 0 & 0 & \cos \theta & 0 & 0 & 0 & \sin \theta & 0 \\ 0 & 0 & 0 & \cos \theta & 0 & 0 & 0 & \sin \theta \\ -\sin \theta & 0 & 0 & 0 & \cos \theta & 0 & 0 & 0 \\ 0 & -\sin \theta & 0 & 0 & 0 & \cos \theta & 0 & 0 \\ 0 & 0 & -\sin \theta & 0 & 0 & 0 & \cos \theta & 0 \\ 0 & 0 & 0 & -\sin \theta & 0 & 0 & 0 & \cos \theta \end{bmatrix}. \quad (18)$$

with collision angle

$$\theta = \frac{\varepsilon}{4n(x, z)} \quad (19)$$

The streaming operator \vec{S} will stream the 8-qubit subset $[\bar{q}_0, \bar{q}_1, \bar{q}_2, \bar{q}_3, \bar{q}_8, \bar{q}_9, \bar{q}_{10}, \bar{q}_{11}]$, while the streaming operator \overleftarrow{S} will stream the remaining 8-qubit subset $[\bar{q}_4, \bar{q}_5, \bar{q}_6, \bar{q}_7, \bar{q}_{12}, \bar{q}_{13}, \bar{q}_{14}, \bar{q}_{15}]$.

To complete the 16-qubit 1D QLA for x-propagation we need to define the potential collision operators that will recover the $\partial n/\partial x$ terms in the (reduced) Eqs. (12)-(13). There will be 2 such potential operators. The first will have block diagonal structure based on the 2×2 matrix

$$P_1(\gamma) = \begin{bmatrix} \cos \gamma & \sin \gamma \\ \sin \gamma & \cos \gamma \end{bmatrix} \quad (20)$$

with

$$\bar{P}_{1X}(\gamma) = \begin{bmatrix} P_1(\gamma) & 0 & 0 & 0 & 0 & 0 & 0 & 0 \\ 0 & P_1(\gamma) & 0 & 0 & 0 & 0 & 0 & 0 \\ 0 & 0 & P_1(\gamma) & 0 & 0 & 0 & 0 & 0 \\ 0 & 0 & 0 & P_1(\gamma) & 0 & 0 & 0 & 0 \\ 0 & 0 & 0 & 0 & P_1(\gamma) & 0 & 0 & 0 \\ 0 & 0 & 0 & 0 & 0 & P_1(\gamma) & 0 & 0 \\ 0 & 0 & 0 & 0 & 0 & 0 & P_1(\gamma) & 0 \\ 0 & 0 & 0 & 0 & 0 & 0 & 0 & P_1(\gamma) \end{bmatrix}. \quad (21)$$

The potential collision angle

$$\gamma = \varepsilon^2 \frac{\partial n / \partial x}{2n^2} \quad (22)$$

$\bar{P}_{1X}(\gamma)$ is Hermitian but not unitary. The second of the potential collision operators, $\bar{P}_{2X}(\gamma)$, is a sparse unitary operator based on two 8×8 subpotential matrices

$$\bar{P}_{2X}(\gamma) = \begin{bmatrix} P_{11}(\gamma) & P_{12}(\gamma) \\ P_{12}(\gamma) & P_{11}(\gamma) \end{bmatrix}. \quad (23)$$

These 8×8 matrices are given by

$$P_{11}(\gamma) = \begin{bmatrix} \cos \gamma & 0 & 0 & 0 & 0 & 0 & 0 & 0 \\ 0 & \cos \gamma & 0 & 0 & 0 & 0 & 0 & 0 \\ 0 & 0 & \cos \gamma & 0 & 0 & 0 & 0 & 0 \\ 0 & 0 & 0 & \cos \gamma & 0 & 0 & 0 & 0 \\ 0 & 0 & 0 & 0 & \cos \gamma & 0 & 0 & 0 \\ 0 & 0 & 0 & 0 & 0 & \cos \gamma & 0 & 0 \\ 0 & 0 & 0 & 0 & 0 & 0 & \cos \gamma & 0 \\ 0 & 0 & 0 & 0 & 0 & 0 & 0 & \cos \gamma \end{bmatrix}. \quad (24)$$

and

$$P_{12}(\gamma) = \begin{bmatrix} 0 & 0 & 0 & 0 & \sin \gamma & 0 & 0 & 0 \\ 0 & 0 & 0 & 0 & 0 & -\sin \gamma & 0 & 0 \\ 0 & 0 & 0 & 0 & 0 & 0 & \sin \gamma & 0 \\ 0 & 0 & 0 & 0 & 0 & 0 & 0 & -\sin \gamma \\ -\sin \gamma & 0 & 0 & 0 & 0 & 0 & 0 & 0 \\ 0 & \sin \gamma & 0 & 0 & 0 & 0 & 0 & 0 \\ 0 & 0 & -\sin \gamma & 0 & 0 & 0 & 0 & 0 \\ 0 & 0 & 0 & \sin \gamma & 0 & 0 & 0 & 0 \end{bmatrix}. \quad (25)$$

3.3 16-qubit QLA for 1D z-propagation

For the 16-qubit vector \bar{Q} an appropriate unitary collision operator which couples the qubits $\bar{q}_0 - \bar{q}_2$, $\bar{q}_1 - \bar{q}_3$, $\bar{q}_4 - \bar{q}_6$, $\bar{q}_5 - \bar{q}_7$, $\bar{q}_8 - \bar{q}_{10}$, $\bar{q}_9 - \bar{q}_{11}$, $\bar{q}_{12} - \bar{q}_{14}$, $\bar{q}_{13} - \bar{q}_{15}$ is derived from the 4×4 block diagonal structure

$$\bar{C}_Z(\theta) = \begin{bmatrix} C_4(\theta) & 0 & 0 & 0 \\ 0 & C_4(\theta)^T & 0 & 0 \\ 0 & 0 & C_4(\theta) & 0 \\ 0 & 0 & 0 & C_4(\theta)^T \end{bmatrix}, \quad (26)$$

with the 4×4 submatrix

$$C_4(\theta) = \begin{bmatrix} \cos \theta & 0 & \sin \theta & 0 \\ 0 & \cos \theta & 0 & \sin \theta \\ -\sin \theta & 0 & \cos \theta & 0 \\ 0 & -\sin \theta & 0 & \cos \theta \end{bmatrix}, \quad (27)$$

with θ given by Eq. (19).

The streaming operator \vec{S}_Z will stream the 8-qubit subset $[\bar{q}_0, \bar{q}_1, \bar{q}_4, \bar{q}_5, \bar{q}_8, \bar{q}_9, \bar{q}_{12}, \bar{q}_{13}]$, while the streaming operator \overleftarrow{S}_Z will stream the remaining 8-qubit subset $[\bar{q}_2, \bar{q}_3, \bar{q}_6, \bar{q}_7, \bar{q}_{10}, \bar{q}_{11}, \bar{q}_{14}, \bar{q}_{15}]$.

To recover the $\partial n/\partial z$ terms in the (reduced) Eqs. (12) - (13) one introduces two potential collision operators. The first of the potential collision operators has a form that mimics the coupling of the unitary collision matrix \overline{C}_Z with its 4×4 diagonal block structure

$$\overline{P}_{1Z}(\gamma') = \begin{bmatrix} P_4(\gamma') & 0 & 0 & 0 \\ 0 & P_4(\gamma') & 0 & 0 \\ 0 & 0 & P_4(\gamma') & 0 \\ 0 & 0 & 0 & P_4(\gamma') \end{bmatrix}, \quad (28)$$

where

$$P_4(\gamma') = \begin{bmatrix} \cos \gamma' & 0 & -\sin \gamma' & 0 \\ 0 & \cos \gamma' & 0 & -\sin \gamma' \\ -\sin \gamma' & 0 & \cos \gamma' & 0 \\ 0 & -\sin \gamma' & 0 & \cos \gamma' \end{bmatrix}, \quad (29)$$

while the second potential collision operator has diagonal-like structure of two 8×8 matrices

$$\overline{P}_{2Z}(\gamma') = \begin{bmatrix} P_{81}(\gamma') & P_{82}(\gamma') \\ P_{82}(\gamma') & P_{81}(\gamma') \end{bmatrix}, \quad (30)$$

where

$$P_{81}(\gamma') = \begin{bmatrix} \cos \gamma' & 0 & 0 & 0 & 0 & 0 & 0 & 0 \\ 0 & \cos \gamma' & 0 & 0 & 0 & 0 & 0 & 0 \\ 0 & 0 & \cos \gamma' & 0 & 0 & 0 & 0 & 0 \\ 0 & 0 & 0 & \cos \gamma' & 0 & 0 & 0 & 0 \\ 0 & 0 & 0 & 0 & \cos \gamma' & 0 & 0 & 0 \\ 0 & 0 & 0 & 0 & 0 & \cos \gamma' & 0 & 0 \\ 0 & 0 & 0 & 0 & 0 & 0 & \cos \gamma' & 0 \\ 0 & 0 & 0 & 0 & 0 & 0 & 0 & \cos \gamma' \end{bmatrix}. \quad (31)$$

and

$$P_{82}(\gamma') = \begin{bmatrix} 0 & 0 & 0 & 0 & 0 & 0 & 0 & -\sin \gamma' \\ 0 & 0 & 0 & 0 & 0 & 0 & -\sin \gamma' & 0 \\ 0 & 0 & 0 & 0 & 0 & -\sin \gamma' & 0 & 0 \\ 0 & 0 & 0 & 0 & -\sin \gamma' & 0 & 0 & 0 \\ 0 & 0 & 0 & \sin \gamma' & 0 & 0 & 0 & 0 \\ 0 & 0 & \sin \gamma' & 0 & 0 & 0 & 0 & 0 \\ 0 & \sin \gamma' & 0 & 0 & 0 & 0 & 0 & 0 \\ \sin \gamma' & 0 & 0 & 0 & 0 & 0 & 0 & 0 \end{bmatrix}. \quad (32)$$

The potential collision angle is similar to that for x-propagation except that now the derivative on the refractive index is with respect to z

$$\gamma' = \varepsilon^2 \frac{\partial n / \partial z}{2n^2}. \quad (33)$$

3.4 16-qubit QLA for 2D x-z propagation

Piecing together the 1D propagation in x and that in z one obtains the 2D QLA acting on the 16-qubit vector. Thus for the x-dependence one has the unitary collide-stream sequence in the x-direction

$$U_X = \bar{S}_- \bar{C}_X \bar{S}_+ \bar{C}_X^\dagger \cdot S_+ \bar{C}_X S_- \bar{C}_X^\dagger \quad (34)$$

$$\bar{U}_X = S_+ \bar{C}_X^\dagger S_- \bar{C}_X \cdot \bar{S}_- \bar{C}_X^\dagger \bar{S}_+ \bar{C}_X. \quad (35)$$

while for z-dependence the corresponding unitary collide-stream structure is

$$U_Z = \bar{S}_- \bar{C}_Z \bar{S}_+ \bar{C}_Z^\dagger \cdot S_{+Z} \bar{C}_Z S_{-Z} \bar{C}_Z^\dagger \quad (36)$$

$$\bar{U}_Z = S_{+Z} \bar{C}_Z^\dagger S_{-Z} \bar{C}_Z \cdot \bar{S}_- \bar{C}_Z^\dagger \bar{S}_+ \bar{C}_Z. \quad (37)$$

The 2D 16-qubit QLA algorithm is simply

$$\bar{Q}(t + \delta t) = \bar{P}_{1Z} \bar{P}_{2Z} \cdot \bar{U}_Z \cdot U_Z \cdot \bar{P}_{1X} \bar{P}_{2X} \cdot \bar{U}_X \cdot U_X \bar{Q}(t) \quad (38)$$

This will recover, in the long time long spatial scale expansion ($\varepsilon \ll 1$) a set of 16 partial differential equations for $[\bar{q}_0, \dots, \bar{q}_{15}]$. One recovers the 8-spinor 2D representation, $[q_0, \dots, q_7]$, of Maxwell equations to $O(\varepsilon^2)$, Eq. (12)-(13), by the identification

$$q_0 = \bar{q}_0 + \bar{q}_2, q_1 = \bar{q}_1 + \bar{q}_3, q_2 = \bar{q}_4 + \bar{q}_6, q_3 = \bar{q}_5 + \bar{q}_7, \quad (39)$$

$$q_4 = \bar{q}_8 + \bar{q}_{10}, q_5 = \bar{q}_9 + \bar{q}_{11}, q_6 = \bar{q}_{12} + \bar{q}_{14}, q_7 = \bar{q}_{13} + \bar{q}_{15}, \quad (40)$$

The initial conditions are the given electromagnetic field components of the pulse at $t = 0$. Using the Riemann-Silberstein-Weber variables we have then the initial condition on the 8-spinor (q_0, \dots, q_7) . The initial condition for the 16-qubit $\bar{Q}(t = 0)$ is just

$$\bar{q}_0 = \bar{q}_2 = q_0/2, q_1 = \bar{q}_1 + \bar{q}_3, q_2 = \bar{q}_4 + \bar{q}_6, q_3 = \bar{q}_5 + \bar{q}_7, \quad (41)$$

$$q_4 = \bar{q}_8 + \bar{q}_{10}, q_5 = \bar{q}_9 + \bar{q}_{11}, q_6 = \bar{q}_{12} + \bar{q}_{14}, q_7 = \bar{q}_{13} + \bar{q}_{15}, \quad (42)$$

We have tested the 1D QLA for all three Cartesian directions of propagation - the 8 qubit representations for x - and y - dependence, as well as the 16 qubit representation for z - propagation. All 3 codes are in extremely good agreement with each other. We have also performed detailed simulations of the reflection and transmission of an electromagnetic pulse as it propagates at normal incidence to dielectric boundary layers with refractive indices changing rapidly (but continuously) from regions of $n_1 = const.$ to $n_2 = const.$. To study multiple reflections and transmission within the dielectric slab n_2 we consider this slab wedged in between a region of dielectric n_1 and enforcing periodic boundary conditions at the end points of the 1D simulation for z-propagation and the 16-qubit QLA.

We have found excellent agreement with standard electromagnetic theory of the normal incidence of a *plane* electromagnetic wave onto a discontinuous dielectric boundary: in particular, excellent agreement between the ratio of the electric to magnetic field component within a given medium, excellent agreement with the phase velocities as well as whether the reflected electric (if $n_2 > n_1$) or magnetic field (if $n_2 < n_1$) undergoes a π - phase change. It should be noted that in standard plane wave propagation incident onto a dielectric interface, jump conditions are enforced while in the 1D QLA we are performing an initial value simulation without any internal boundary conditions. To model the plane wave discontinuous, one requires that the dielectric boundary layer

be considerably smaller than the width of the pulse. The only difference with plane wave electromagnetics is in the ratio of the transmitted to incident electric fields : plane wave theory yields $2n_1/(n_1 + n_2)$ while for pulse propagation the QLA simulations we [29] find

$$\frac{E_2}{E_1} = \frac{2n_1}{n_1 + n_2} \cdot \sqrt{\frac{n_2}{n_1}} \quad (43)$$

where the pulse is moving from refractive index $n_1 \rightarrow n_2$. Moreover the QLA pulse rigorously satisfies the conservation of Poynting flux - even during those time periods in which the pulse is straddling the boundary layer and has parts of it in n_1 -regions as well as in the n_2 -region. We have developed a theory on Gaussian pulses that indeed show that E_2/E_1 does indeed satisfy Eq. (43).

4 2D QLA SIMULATIONS

QLA simulations will be presented for the interaction of an initially 1D Gaussian pulse propagating in the x - direction with, in Sec. 4.1, a small cylindrical 2D dielectric with refractive index $n(x, z)$, and in Sec. 4.2 a small 2D conic dielectric.

4.1 Gaussian Pulse interacting with a 2D Dielectric Cylinder

4.1.1 Electric Field

Consider a 1D Gaussian electromagnetic pulse propagating in the x - direction with non-zero field components $E_y(x, t = 0)$ and $B_z(x, t = 0)$, towards a dielectric cylinder with peak refractive index $n = 2$ - Fig. 1.

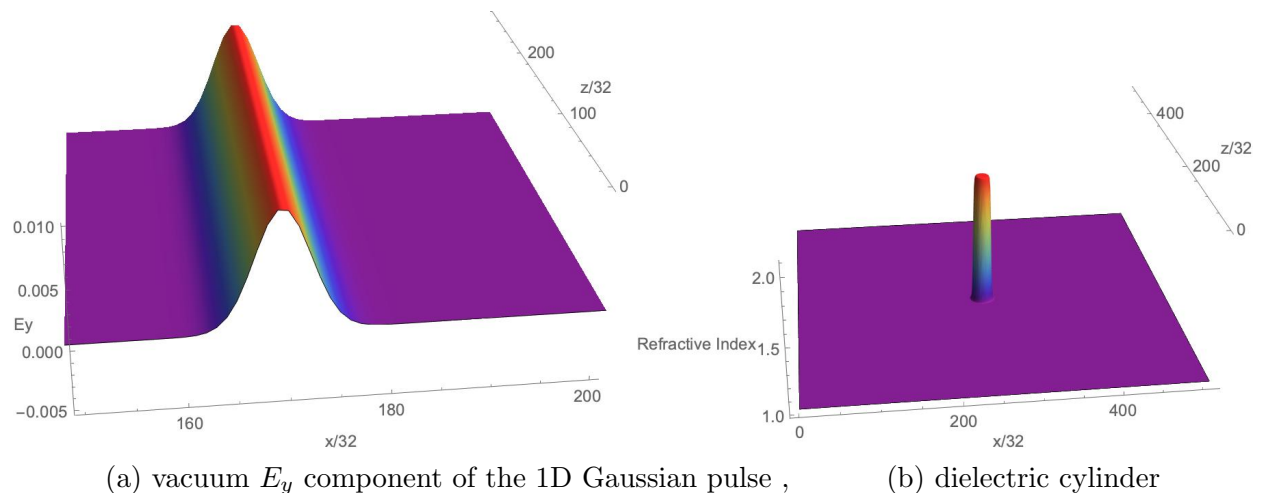


Figure 1: (a) The E_y of the initial electromagnetic pulse, (b) the refractive index $n(x, z)$. Grid 16384^2 . The plots are from data at every 32nd point in each direction, leading to a full simulation domain of $0 < x/32, z/32 \leq 512$. We ourselves perform no smoothing of the data.

At $t = 16k$, (i.e., after 16000 iterations), the pulse starts its interaction with the dielectric cylinder. A part of the pulse will be reflected, a part transmitted into the dielectric, while the major part of the pulse will just continue to propagate in the vacuum. In Fig, 2a one sees a blowup

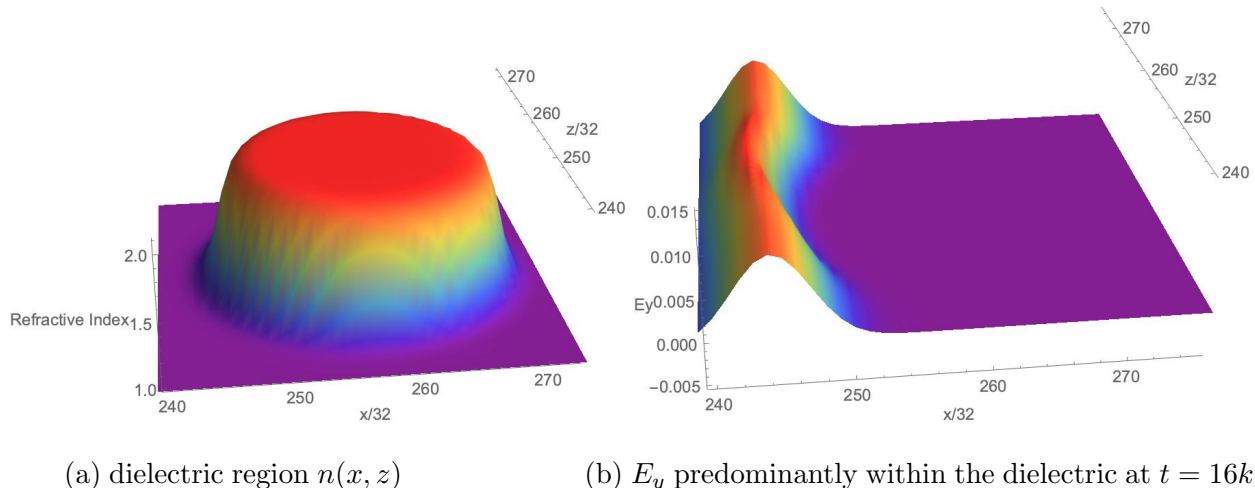


Figure 2: (a) a blowup of the dielectric region and (b) the E_y field in this region at time $t = 16k$ as the pulse starts interacting with the dielectric. The phase velocity within the dielectric region is less than its speed in the vacuum and hence the concave bend in the pulse within the dielectric. The plots are of the limited spatial domain $240 \leq x/32, z/32 \leq 272$ of the dielectric.

of the dielectric region, while in Fig. 2b, we see the beginnings of 2D features in the interaction of the pulse with the dielectric cylinder.

At $t = 18k$, we see a weak reflection from the dielectric cylinder and a quite strong transmission into the dielectric region (Fig. 3a). In the weak reflection back into the vacuum one notices that here predominantly is a ring with $E_y < 0$ - somewhat reminiscent of the 1D result when a pulse is moving from low to higher refractive index. The strong concave structure of the pulse within the dielectric arises from its slower phase velocity than in a vacuum, while the width of the pulse within the dielectric is similarly reduced. By $t = 21k$ that part of the pulse in the dielectric is reaching the boundary layer with the vacuum. Part of this pulse will be transmitted into the vacuum while another part will be reflected back into the dielectric traveling to the left, as seen in Fig. 4a at time $t = 23k$ and in Fig. 4b, time $t = 25k$. This is followed by another reflection/transmission shown in Fig. 5.

With these repeated transmissions/reflections the outgoing pulses from the dielectric region into the vacuum are quite complex, as seen in Fig. 6. Here we plot the complete domain of the data $0 \leq x/32, z/32 \leq 512$. That part of the pulse that remains 1D as it propagates past the dielectric is clearly seen,

In Fig. 7, we show at $t = 40k$ both the positive and negative aspect of $E_y(x, z)$. It should be noted the only non-zero component of the electric field throughout this 2D simulation is the $E_y(x, z)$ - component.

4.1.2 The generated B_x magnetic field and $\nabla \cdot \mathbf{B}$

Initially, for the 1D Gaussian pulse propagating in the x -direction the only non-zero component of the magnetic field is $B_z(x)$. Trivially, $\nabla \cdot \mathbf{B} = \mathbf{0}$. However, once the interaction between the pulse and the dielectric occurs we will find a $B_x(x, z, t)$ being generated along with the B_z taking on (x, z) -dependence. This is necessary for $\nabla \cdot \mathbf{B} = \mathbf{0}$. There is no B_x field for $t < 16k$. In Fig. 8 we show the $B_x(x, z)$ field from both the positive and negative perspective, clearly showing its dipole structure. At later times ($t = 40k$), the dipole structure of B_x is still apparent, Fig. 9.

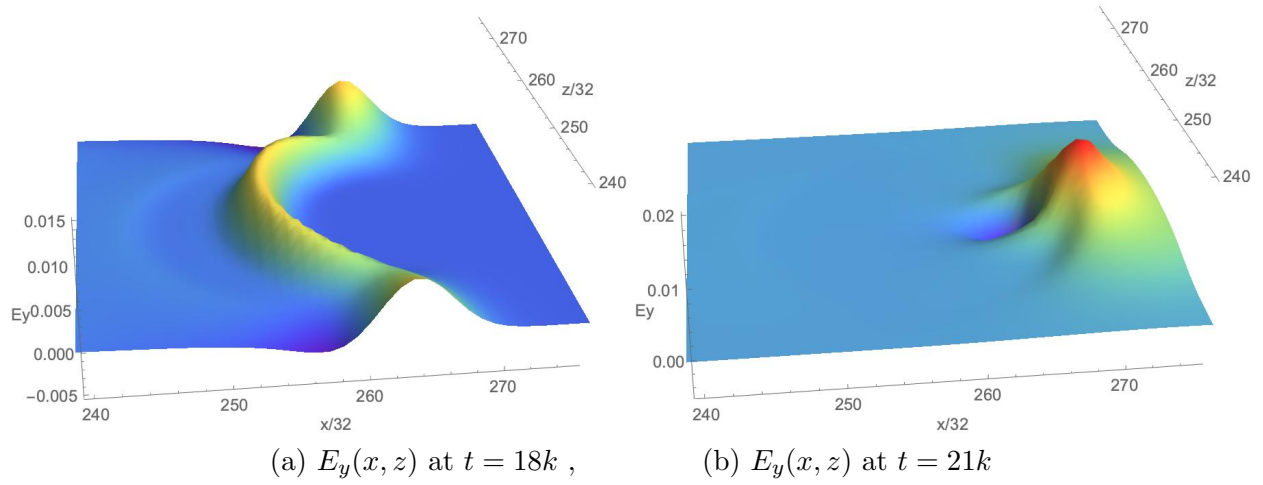


Figure 3: The E_y field predominantly within the dielectric at (a) $t = 18k$, (b) $t = 21k$ as the pulse is propagating in \rightarrow direction. Un (b), the pulse is near the dielectric-vacuum boundary layer.

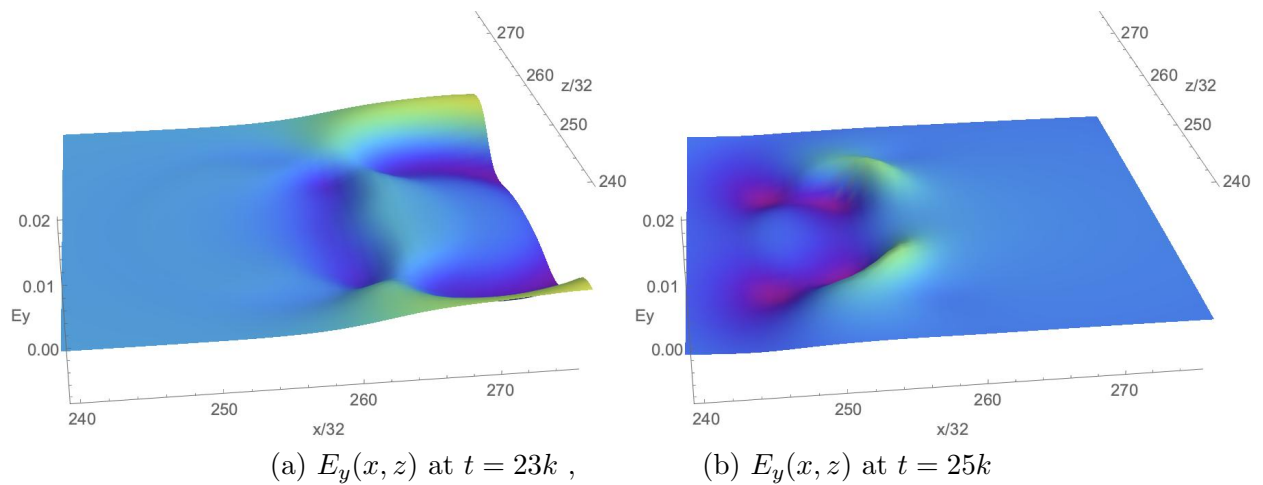


Figure 4: The E_y field predominantly within the dielectric at (a) $t = 23k$, (b) $t = 25k$ as the pulse is propagating in \leftarrow direction.

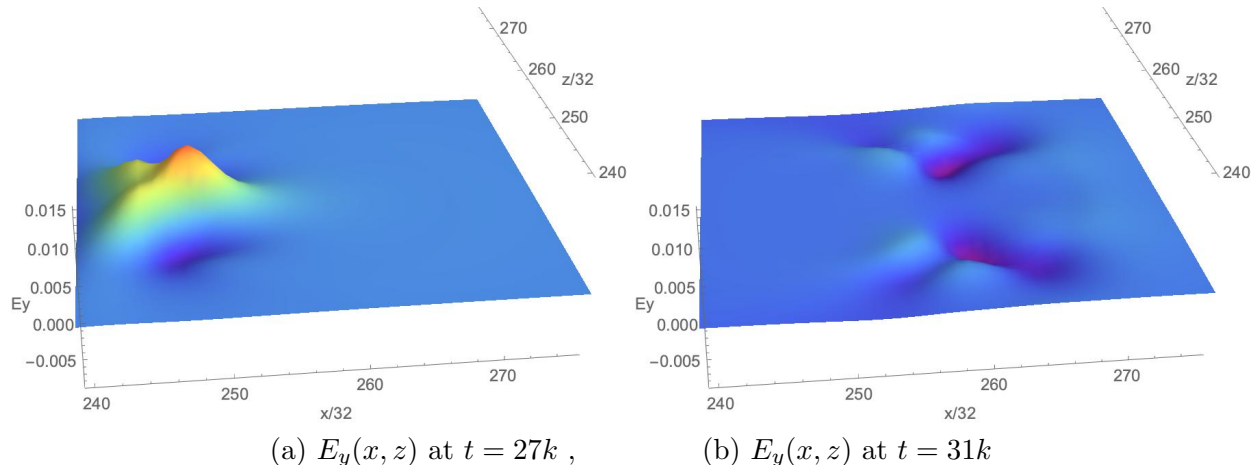


Figure 5: The E_y field predominantly within the dielectric at (a) $t = 27k$, with the pulse traveling \leftarrow , but now close to the vacuum boundary while at (b) $t = 31k$ the E_y of the reflected pulse propagating is \rightarrow and shows significant regions of $E_y < 0$.

Finally we show the field $\nabla \cdot \mathbf{B}$ for early times ($t = 15k$) and towards the end of the simulation ($t = 40k$), Figs. 10 and 11.

There does not seem to be any contamination of the very small non-zero $\nabla \cdot \mathbf{B}$ in the time evolution of the electromagnetic pulse. This is possibly due to the fact that one is solving for the electromagnetic field in a mesoscopic 16– qubit representation rather than with the electromagnetic fields themselves.

4.2 1D Pulse Propagation into a Conic Dielectric with slowly varying refractive index.

We now consider the effect of weaker spatial gradients in the boundary layer of the dielectric medium on the reflection/transmission of the 1D Gaussian pulse. In particular, a magnified view of the dielectric cone is shown in Fig. 12a for asymptotic regions of $n_1 = 1$ to a peak in $n_{2,max} = 2$. In Fig. 12b we see the corresponding dielectric cone if the peak in n_2 is $n_{2,max} = 3$.

For the peak $n_{2,max} = 2$ dielectric, the gradients in the refractive index are so gentle that there are no perceptible reflections of the pulse within the dielectric region. This results in a most simple single outgoing wavefront into the vacuum (Fig 13a). For the steeper gradient dielectric profile, Fig 12b, we do see the effect of an internal reflection within the dielectric cone, resulting in the double wavefront seen in Fig. 13b. These wavefronts are much simpler than that seen for a strongly varying boundary layer cylindrical dielectric (Fig. 7)

The corresponding B_x generated by the scattering at $t = 40k$ is shown in Fig. 14, while $\nabla \cdot \mathbf{B}$ is shown in Fig. 15.

4.3 The perturbation parameter ε in QLA

QLA recovers the Maxwell equations to $O(\varepsilon^2)$ where ε is introduced as a small parameter into the unitary operator collision angle, Eqs. 19. All the simulations reported in this paper have been for $\varepsilon = 0.3$. In our previous QLA for the nonlinear Schrodinger equation and for the (3D) spinor Bose-Einstein condensate equations, ε was related to the soliton/quantum vortex amplitude. For

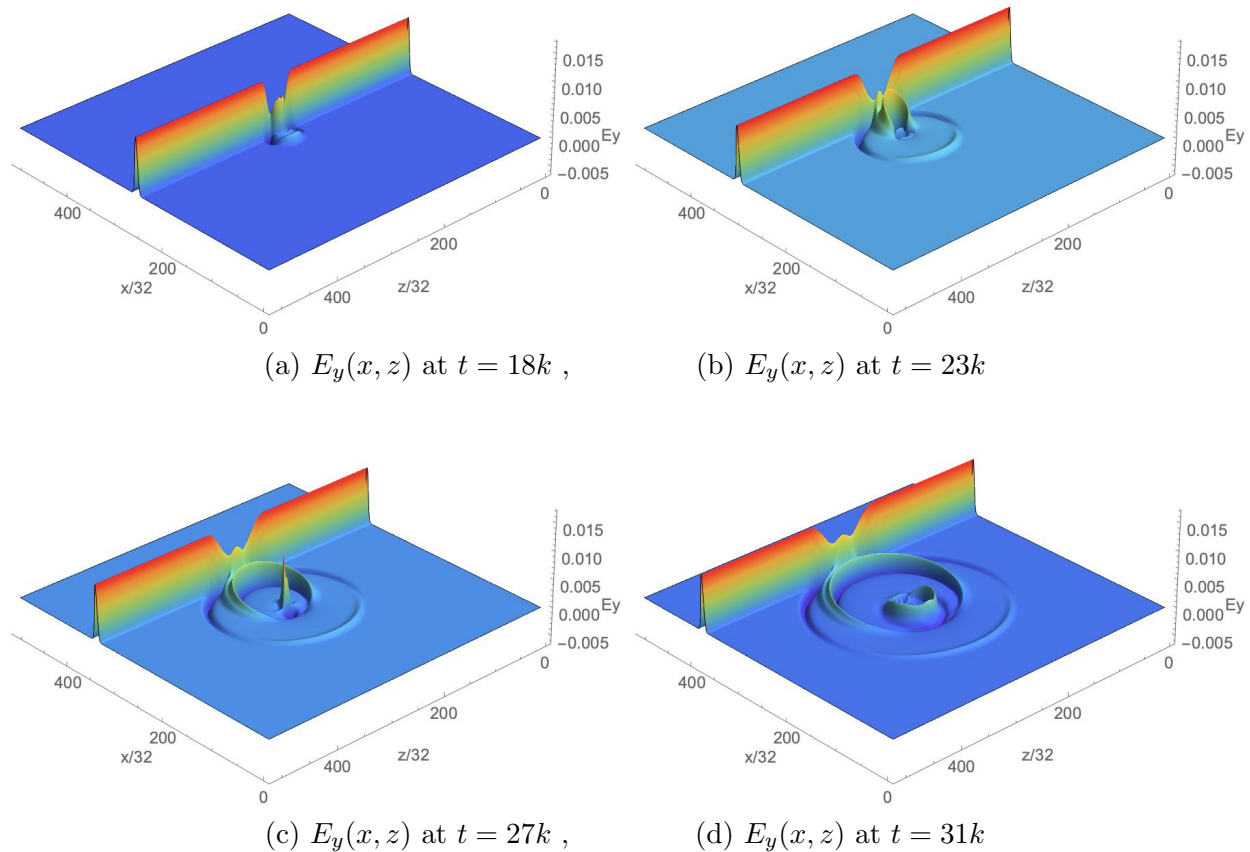


Figure 6: The total E_y field at (a) $t = 18k$, (b) $t = 23k$, (c) $t = 27k$, and (d) $t = 31k$. The 1D initial pulse retains much of its 1D structure away from the dielectric region. However the internal reflections and transmissions within the dielectric cylinder results in quite complex circular wavefronts propagating into the vacuum. The initial ring shows significant portions in which $E_y < 0$ around the back part of the cylindrical dielectric.

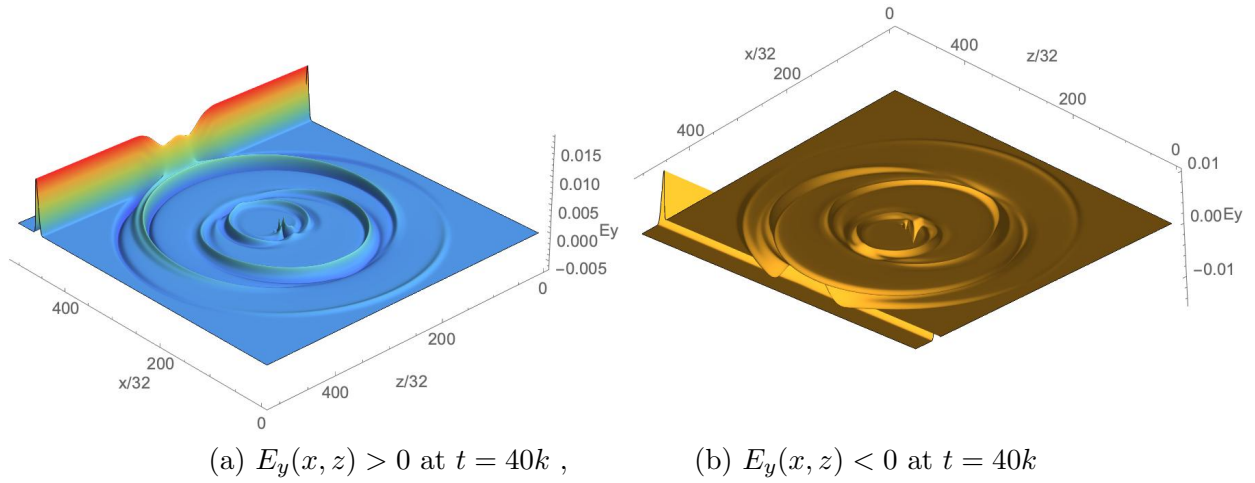


Figure 7: The E_y field at $t = 40k$ from (a) a positive $E_y > 0$ perspective, and from (b) a negative $E_y < 0$ perspective.

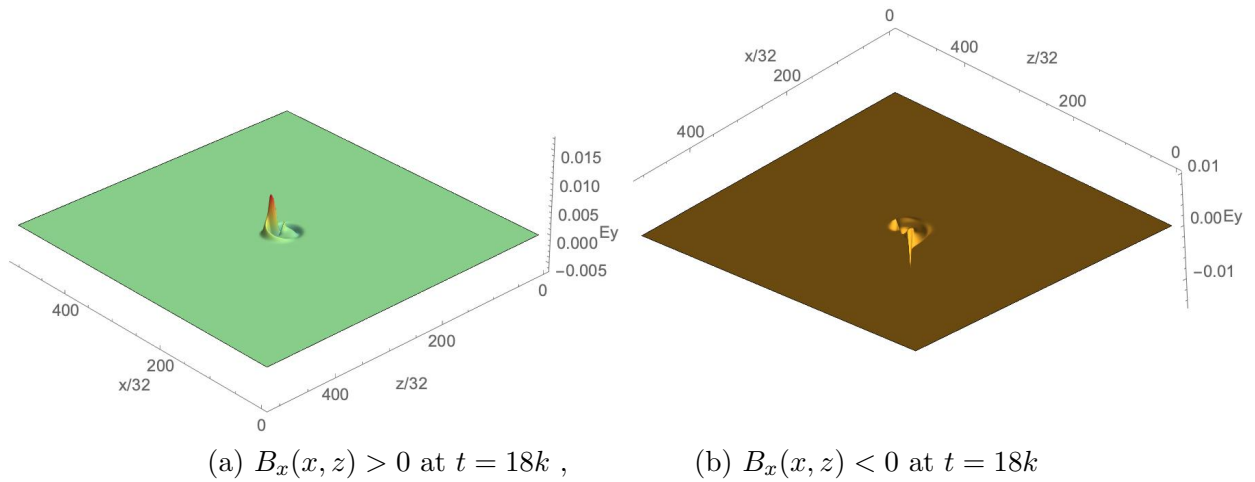


Figure 8: The $B_x(x, z)$ field at $t = 18k$ showing its beginnings as a dipole structure: (a) a positive $B_x > 0$ perspective, and from (b) a negative $B_x < 0$ perspective.

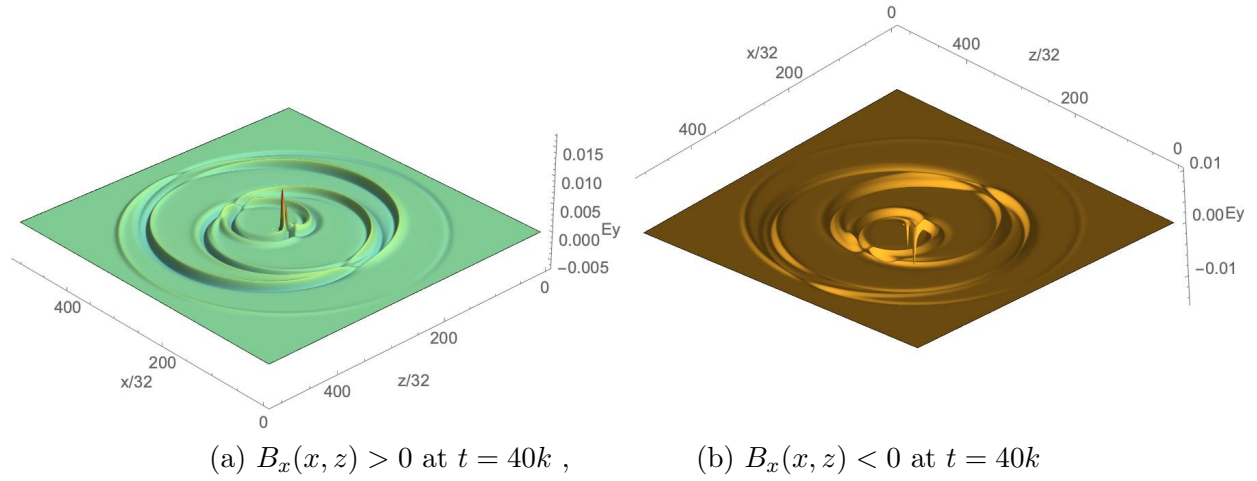


Figure 9: The $B_x(x, z)$ field at $t = 40k$ with its strong dipole structure: (a) a positive $B_x > 0$ perspective, and from (b) a negative $B_x < 0$ perspective. As expected, there are no B_x components generated directly by those of the 1D Gaussian pulse.

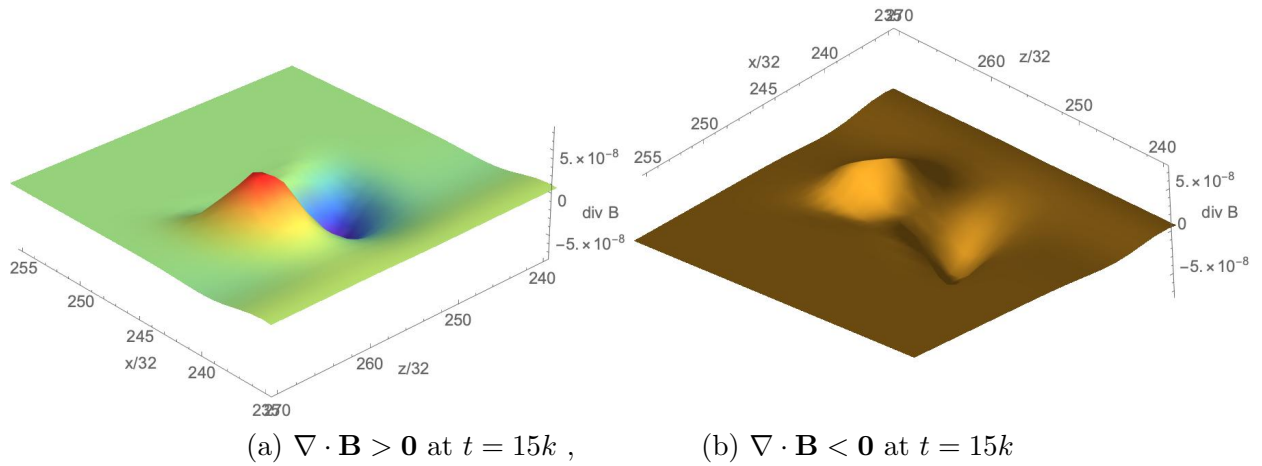


Figure 10: The $\nabla \cdot \mathbf{B}$ field at $t = 15k$ with a very weak dipole structure: (a) a positive $\nabla \cdot \mathbf{B}$ perspective, and from (b) a negative $\nabla \cdot \mathbf{B}$ perspective.. Notice the maximum scaling of 5×10^{-8} .

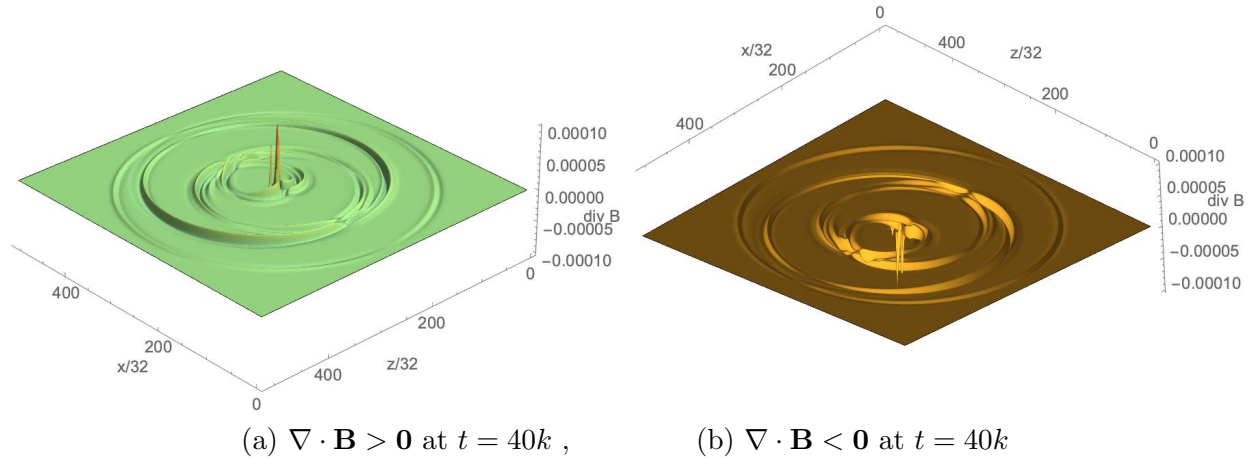


Figure 11: The $\nabla \cdot \mathbf{B}$ field at $t = 40k$ with its dipole structure: (a) a positive $\nabla \cdot \mathbf{B}$ perspective, and from (b) a negative $\nabla \cdot \mathbf{B}$ perspective.. Now the very localized peak maximum is 2 orders of magnitude below the corresponding peak in B_z . Away from these peaks, $\nabla \cdot \mathbf{B}$ becomes much smaller.

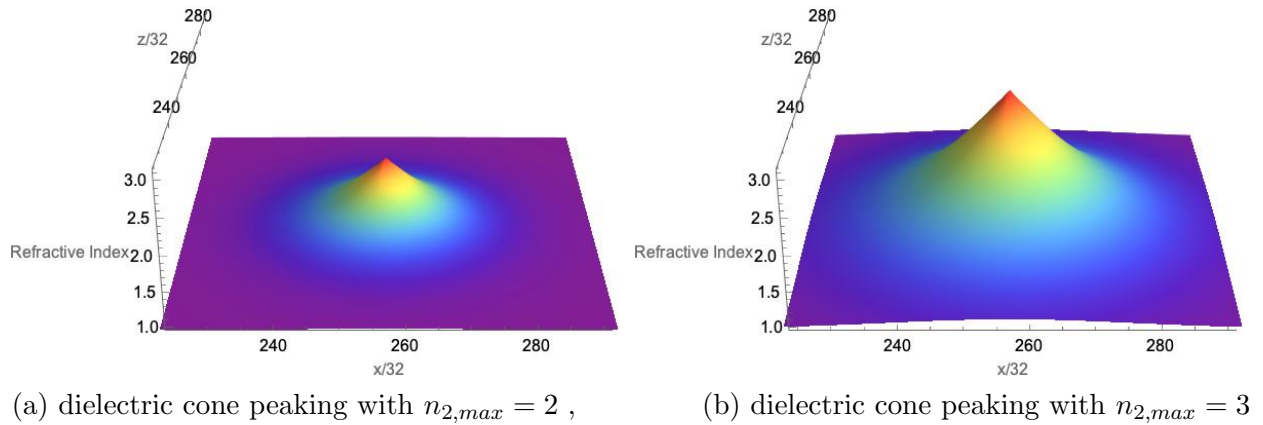


Figure 12: Two different scattering scenarios for a 1D Gaussian vacuum ($n_1 = 1$) pulse propagating to a dielectric cone.

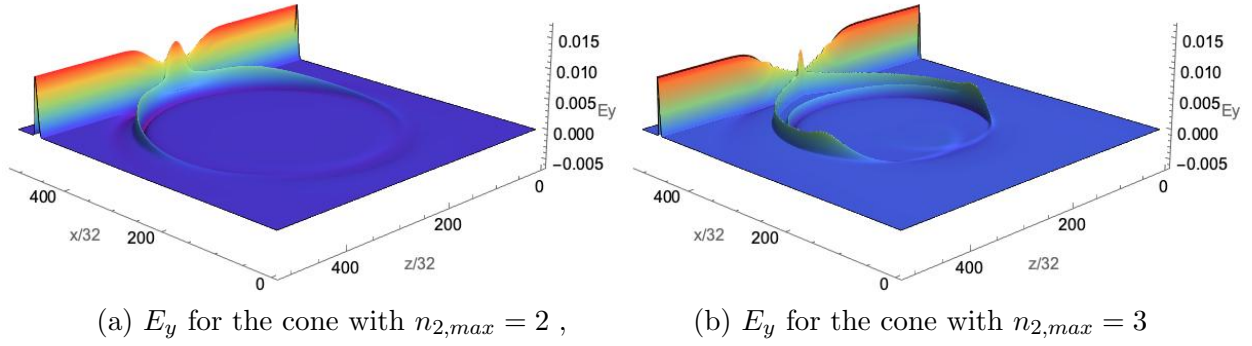


Figure 13: The long time effect of the interaction of a 1D Gaussian pulse with a dielectric cone. These wavefronts should be compared with the corresponding wave front for scattering of the 1D pulse off a dielectric cylinder, Fig. 7

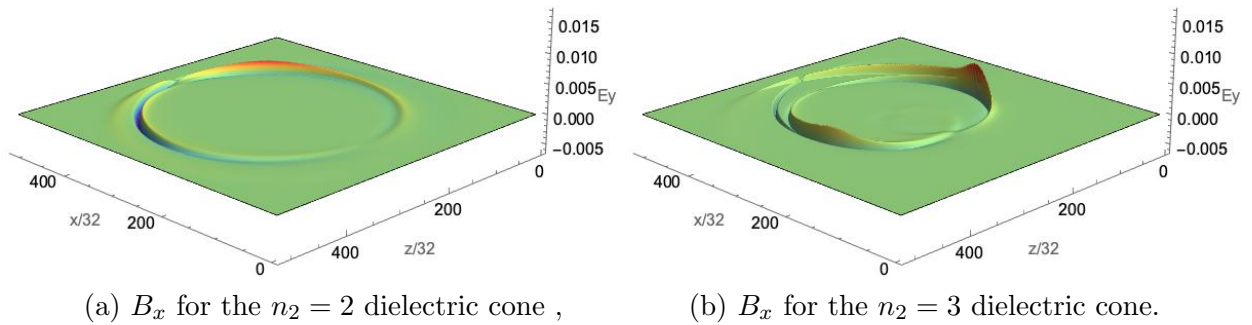


Figure 14: Two different scattering scenarios for a 1D Gaussian vacuum ($n_1 = 1$) pulse propagating to a dielectric cone. The differences in the cone dielectrics is seen in Fig. 12.

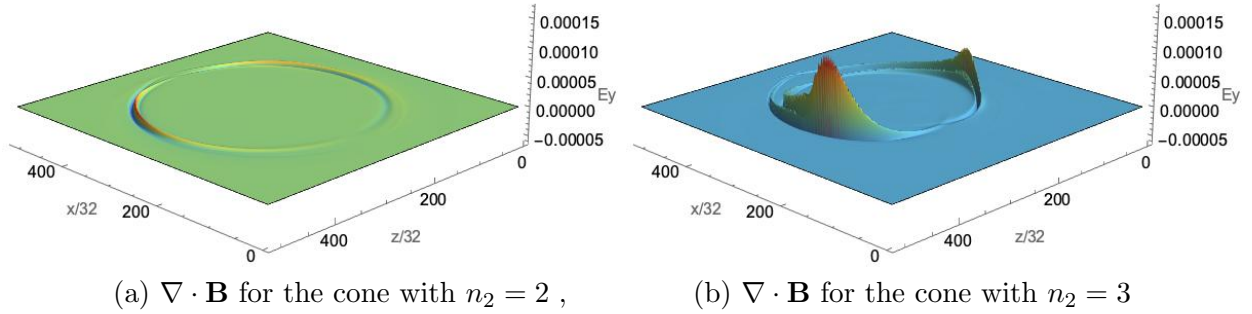


Figure 15: Two different scattering scenarios for a 1D Gaussian vacuum ($n_1 = 1$) pulse propagating to a dielectric cone (see Fig. 12 for more details). $\nabla \cdot \mathbf{B}$ is zero everywhere except in a circle ring. (a) For very weak dielectric gradients $\nabla \cdot \mathbf{B}/|\mathbf{B}| \ll 10^{-3}$, while for steeper gradients, Fig 12(b), in a few regions $\nabla \cdot \mathbf{B}/|\mathbf{B}| = 10^{-2}$,

these nonlinear problems, simulations of these QLA models revealed an upper bound to ε_{max} above which the QLA solutions were no longer recovering the appropriate soliton/quantum vortex time behavior. This is the well known price one is forced to pay when applying perturbation theory.

For the linear Maxwell equations, we find that the collision angle perturbation parameter ε in our QLA representation is nothing but the normalized speed of the initial electromagnetic pulse. Somewhat unexpectedly, when performing QLA simulations even to $\varepsilon = 1$, the QLA is still recovering Maxwell equations in the continuum limit. In Fig. 16 we plot the E_y and the B_z fields at $t = 40k$. These field should be compared to the $\varepsilon = 0.3$ QLA solutions in Figs. 7a and 9a.

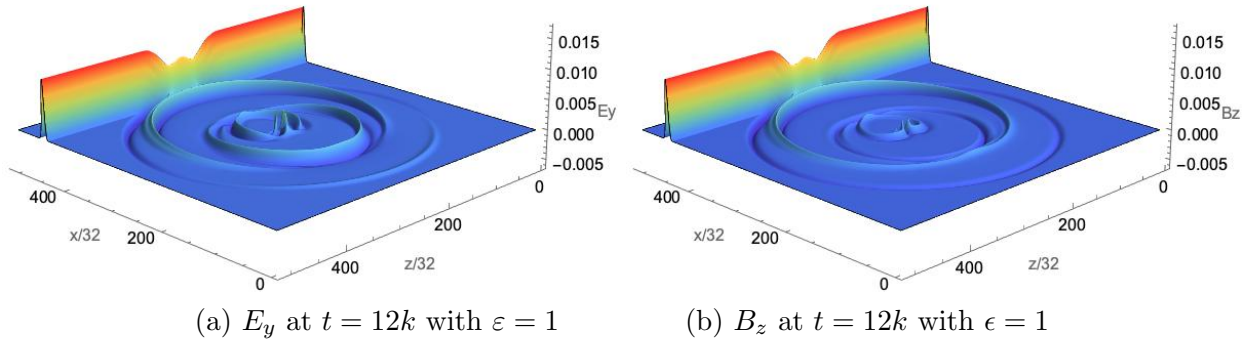


Figure 16: The effect of the dielectric cylinder on a 1D x-propagating Gaussian pulse at large times. QLA simulations with $\varepsilon = 1$, for the E_y and B_z fields at $t = 12k$. (a) should be contrasted with the corresponding E_y field in Figs. 7a obtained from the QLA with $\varepsilon = 0.3$.

Again, as the initial pulse becomes 2D following its interaction with the dielectric cylinder, a $B_x(x, z)$ must be generated so that $\nabla \cdot \mathbf{B} = 0$ is not violated. The fields, for $\varepsilon = 1$ should be compared to the corresponding fields in Fig. 9a and 11a at $t = 40k$ at $\varepsilon = 0.3$. Of course, there is an obvious computational advantage of running at $\varepsilon = 1.0$ over at $\varepsilon = 0.3$: a wall clock time

reduction of over 3.3. The 2D QLA simulations were run on a 16384×16384 grid on 8192 Cori Haswell cores. The wall clock time with $\varepsilon = 0.3$ was 4.05 hrs for 100 data dumps of 5 fields. The data is plotted on a $x/32 \times z/32$ grid - i.e., on a 512×512 grid and we ourselves perform no smoothing of the data.

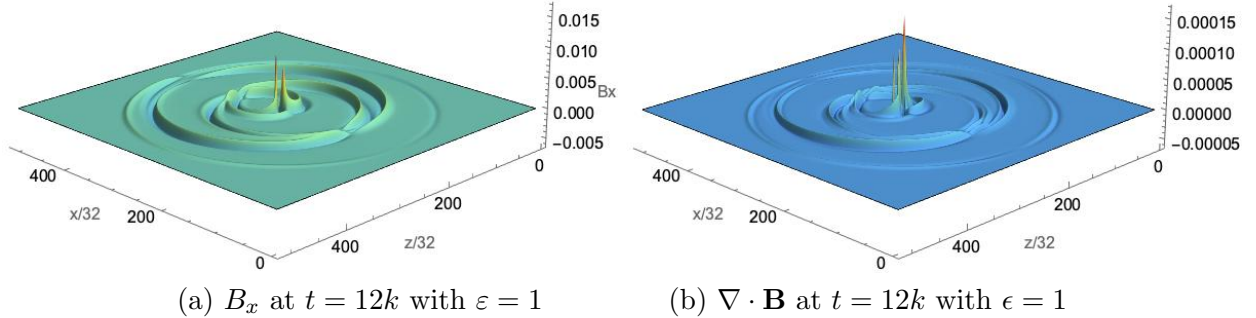


Figure 17: The effect of the dielectric cylinder, Fig. 1b, on a 1D x-propagating Gaussian pulse at large times ($t = 12k$) with $\varepsilon = 1$. (a) B_x , (b) $\nabla \cdot \mathbf{B}$.

5 Summary and Conclusions

We have performed detailed QLA simulations of the scattering of an electromagnetic pulse off a localized 2D scalar dielectric medium. If the strength of the spatial gradient of the dielectric boundary layer is large, we find reflections/transmissions of the pulse within the dielectric. This leads to the dielectric emitting outgoing wavefronts into the vacuum like a quasi-antenna. If the spatial gradients are weak, the pulse's interaction with the dielectric resembles small angle scattering of a WKB ray.

In our current formulation of the Maxwell equations, we are only solving $\nabla \cdot \mathbf{B} = 0$ to second order in the unitary collision angle parameter ε . Nevertheless we do not seem to be tainted by this in the simulations. A possible reason for this is that QLA is a mesoscopic representation and the Maxwell equations are recovered in the continuum limit. Hence the time evolution of the QLA simulation does not deal directly with the magnetic field \mathbf{B} .

QLA's are necessarily perturbative theories since only in extremely rare cases can one perform a closed form representation of the collision matrix. In our earlier work on solving the 1D Nonlinear Schrodinger equation (*NLS*) or the 2D and 3D Gross-Pitaevskii equation for the evolution of a Bose-Einstein condensate (*BEC*) ground state or the further generalizations to spinor BECs, the perturbation parameter in the collision operators was related to the amplitude of the wave function. The QLA recovers the desired continuum equations perturbatively, and QLA simulations have determined an ε_{max} above which the QLA simulations do not yield solutions to the desired continuum equations. For example, in 1D NLS, one recovers the exact soliton-soliton collision features for $\varepsilon < \varepsilon_{max}$. However, if we choose $\varepsilon > \varepsilon_{max}$ one sees the soliton breakdown in time. All this is saying is that the QLA is now representing an equation different from 1D NLS - because of the choice of too high an ε . In our QLA representation of the Maxwell equations in scalar media, we find that the ε is just the normalized speed of light in that medium. Our simulations show that the QLA holds for Maxwell equations even for $\varepsilon = 1$.

Finally QLA can be viewed from 2 sides: on the one side it is basically a unitary qubit lattice representation of Maxwell equations which should be able to be run on error-correcting quantum machines as they come on-line. It has been noticed by Khan that the structure of Maxwell equations in a scalar dielectric medium are non-unitary: the evolution operators that involve the derivative on the dielectric function are Hermitian, and not unitary. In our QLA this is seen in our potential collision operators being non-unitary. This will make the application of quantum algorithms for plasma physics to be more challenging since clever constructs need to be performed in order to still represent such non-unitary systems on a quantum computer [30]. Similar comments can be made on how to represent nonlinear physics on a linear quantum mechanical computer. Nearly every interesting nonlinear problem cannot be simply transformed into a linear system. The other side of looking at QLA is that it is an ideally parallelized algorithm to run on classical supercomputers. Indeed our QLA spinor BEC codes did not see saturation with nodes on the IBM *Mira* machine, even up to the maximum 786,432 cores available to us (in 2015). This is also why we have run on such large grids for our Maxwell equations: it is basically to test out and tune the algorithm as we move to harder and harder problems.

6 Acknowledgments

This research was partially supported by Department of Energy grants DE-SC0021647, DE-FG02-91ER-54109, DE-SC0021651, DE-SC0021857, and DE-SC0021653. The simulations were performed on *CORI* of the National Energy Research Scientific Computing Center (NERSC), A U.S. Department of Energy Office of Science User Facility located at Lawrence Berkeley National Laboratory, operated under Contract No. DE-AC02-05CH11231.

7 References

- [1] YEPEZ, J. 2002 An efficient and accurate quantum algorithm for the Dirac equation. arXiv: 0210093.
- [2] YEPEZ, J. 2005 Relativistic Path Integral as a Lattice-Based Quantum Algorithm. *Quant. Info. Proc.* 4, 471-509.
- [3] YEPEZ, J, VAHALA, G & VAHALA, L. 2009a Vortex-antivortex pair in a Bose-Einstein condensate, Quantum lattice gas model of theory in the mean-field approximation. *Euro. Phys. J. Special Topics* 171, 9-14
- [4] YEPEZ, J, VAHALA, G, VAHALA, L & SOE, M. 2009b Superfluid turbulence from quantum Kelvin wave to classical Kolmogorov cascades. *Phys. Rev. Lett.* 103, 084501.
- [5] YEPEZ, J. 2016 Quantum lattice gas algorithmic representation of gauge field theory. *SPIE* 9996, paper 9996-22
- [6] OGANESOV, A, VAHALA, G, VAHALA, L, YEPEZ, J & SOE, M. 2016a. Benchmarking the Dirac-generated unitary lattice qubit collision-stream algorithm for 1D vector Manakov soliton collisions. *Computers Math. with Applic.* 72, 386
- [7] OGANESOV, A, FLINT, C, VAHALA, G, VAHALA, L, YEPEZ, J & SOE, M 2016b Imaginary time integration method using a quantum lattice gas approach. *Rad Effects Defects Solids* 171, 96-102
- [8] OGANESOV, A, VAHALA, G, VAHALA, L & SOE, M. 2018. Effects of Fourier Transform on the streaming in quantum lattice gas algorithms. *Rad. Eff. Def. Solids*, 173, 169-174
- [9] VAHALA, G, VAHALA, L & YEPEZ, J. 2003 Quantum lattice gas representation of some classical solitons. *Phys. Lett A* 310, 187-196

- [10] VAHALA, G, VAHALA, L & YEPEZ, J. 2004. Inelastic vector soliton collisions: a lattice-based quantum representation. *Phil. Trans: Mathematical, Physical and Engineering Sciences*, The Royal Society, 362, 1677-1690
- [11] VAHALA, G, VAHALA, L & YEPEZ, J. 2005 Quantum lattice representations for vector solitons in external potentials. *Physica A*362, 215-221.
- [12] VAHALA, G, YEPEZ, J, VAHALA, L, SOE, M, ZHANG, B, & ZIEGELER, S. 2011 Poincaré recurrence and spectral cascades in three-dimensional quantum turbulence. *Phys. Rev. E*84, 046713
- [13] VAHALA, G, YEPEZ, J, VAHALA, L & SOE, M, 2012 Unitary qubit lattice simulations of complex vortex structures. *Comput. Sci. Discovery* 5, 014013
- [14] VAHALA, G, ZHANG, B, YEPEZ, J, VAHALA, L & SOE, M. 2012 Unitary Qubit Lattice Gas Representation of 2D and 3D Quantum Turbulence. Chpt. 11 (pp. 239 - 272), in *Advanced Fluid Dynamics*, ed. H. W. Oh, (InTech Publishers, Croatia)
- [15] VAHALA, G, VAHALA, L & SOE, M. 2020. Qubit Unitary Lattice Algorithm for Spin-2 Bose Einstein Condensates: I – Theory and Pade Initial Conditions. *Rad. Eff. Def. Solids* 175, 102-112
- [16] VAHALA, G, SOE, M & VAHALA, L. 2020 Qubit Unitary Lattice Algorithm for Spin-2 Bose Einstein Condensates: II – Vortex Reconnection Simulations and non-Abelian Vortices. *Rad. Eff. Def. Solids* 175, 113-119
- [17] VAHALA, G, VAHALA, L, SOE, M & RAM, A, K. 2020. Unitary Quantum Lattice Simulations for Maxwell Equations in Vacuum and in Dielectric Media, *J. Plasma Phys* **86**, 905860518
- [18] VAHALA, L, VAHALA, G & YEPEZ, J. 2003 Lattice Boltzmann and quantum lattice gas representations of one-dimensional magnetohydrodynamic turbulence. *Phys. Lett A*306, 227-234.
- [19] VAHALA, L, SOE, M, VAHALA, G & YEPEZ, J. 2019a. Unitary qubit lattice algorithms for spin-1 Bose-Einstein condensates. *Rad Eff. Def. Solids* 174, 46-55
- [20] VAHALA, L, VAHALA, G, SOE, M, RAM, A & YEPEZ, J. 2019b. Unitary qubit lattice algorithm for three-dimensional vortex solitons in hyperbolic self-defocusing media. *Commun Nonlinear Sci Numer Simulat* 75, 152-159
- [21] DODIN, I. Y. & STARTEV, E. A. 2021 On applications of quantum computing to plasma simulations. *Phys. Plasmas* **28**, 092101
- [22] ENGEL, A., SMITH, G & PARKER, S. E. 2019 Quantum Algorithm for the Vlasov Equation =. *Phys. Rev.* **100**, 062315
- [23] ENGEL, A., SMITH, G & PARKER, S. E. 2021. Linear Embedding of nonlinear dynamical systems and prospects for efficient quantum algorithms. *Phs Plasmas* **28**, 062305
- [24] LIU, J-P, KOLDEN, H.O, KROVI, H. K, LOUREIRO, N. F, TRIVISA, K, & CHILDS, A. M. 2021. *Proc Natl. Acad. Sciences* **118**, e2026805118.
- [25] LAPORTE, O. & UHLENBECK, G. E. 1931 Application of spinor analysis to the Maxwell and Dirac equations. *Phys. Rev.* **37**, 1380-1397.
- [26] OPPENHEIMER, J. R. 1931 Note on light quanta and the electromagnetic field. *Phys. Rev.* **38**, 725-746.
- [27] MOSES, E. 1959 Solutions of Maxwell's equations in terms of a spinor notation: the direct and inverse problems. *Phys. Rev.* **113**, 1670-1679
- [28] KHAN, S. A. 2005 Maxwell Optics: I. An exact matrix representation of the Maxwell equations in a medium. *Physica Scripta* **71**, 440-442; also arXiv: 0205083v1 (2002)
- [29] RAM, A. K., VAHALA, G., VAHALA, L. & SOE, M 2021 Reflection and transmission of electromagnetic pulses at a planar dielectric interface - theory and quantum lattice simulations *AIP Advances* (submitted) , arXiv:2108.06880.

[30] CHILDS, A, N & WIEBE, N. 2012. Hamiltonian simulation using linear combinations of unitary operations. *Quantum Info. Comput.*12, 901–924.